nature nanotechnology

ARTICLES

PUBLISHED ONLINE: 17 APRIL 2017 | DOI: 10.1038/NNANO.2017.50

Controlling propagation and coupling of waveguide modes using phase-gradient metasurfaces

Zhaoyi Li[1], Myoung-Hwan Kim[1,2†], Cheng Wang[3†], Zhaohong Han[4], Sajan Shrestha[1], Adam Christopher Overvig[1], Ming Lu[5], Aaron Stein[5], Anuradha Murthy Agarwal[4], Marko Lončar[3] and Nanfang Yu[1*]

Research on two-dimensional designer optical structures, or metasurfaces, has mainly focused on controlling the wavefronts of light propagating in free space. Here, we show that gradient metasurface structures consisting of phased arrays of plasmonic or dielectric nanoantennas can be used to control guided waves via strong optical scattering at subwavelength intervals. Based on this design principle, we experimentally demonstrate waveguide mode converters, polarization rotators and waveguide devices supporting asymmetric optical power transmission. We also demonstrate all-dielectric on-chip polarization rotators based on phased arrays of Mie resonators with negligible insertion losses. Our gradient metasurfaces can enable small-footprint, broadband and low-loss photonic integrated devices.

Photonic integrated circuits offer an attractive platform for optical information processing[1–4] and on-chip chemical and biological sensing[5,6]. However, major challenges still exist at the device level that prevent reliable, large-scale system integration. These challenges include miniaturizing device footprints, increasing device operation bandwidth and robustness, and reducing device insertion losses[1–4]. Integration of optical waveguides and gradient metasurface structures may help address some of these challenges.

The basic concept of metasurfaces is to use arrays of antennas with subwavelength separation and spatially varying geometric parameters (for example, antenna shape, size and orientation) to form a heterogeneous distribution of optical response (for example, phase, amplitude, polarization and optical impedance) that can be used to control the propagation of light at will[7–10]. The focus of investigations so far has been on the physics[11–13] and applications[14–17] of using metasurfaces to control light propagating in free space. Recently, metasurfaces have emerged as a way to control guided waves[18–22] and to couple guided waves with waves propagating in free space[23–25].

Across an antenna resonance, the phase of the scattered light wave from an optical nanoantenna relative to that of the incident light wave sweeps a range of ~π (refs 7, 9). A gradient metasurface consists of an array of dissimilar nanoantennas with a constant phase difference $d\Phi$ and a subwavelength separation dx between adjacent elements. The gradient metasurface introduces a unidirectional phase gradient $d\Phi/dx$, equivalent to a unidirectional effective wavevector $\mathbf{k}_{\mathrm{eff}}$, along the surface and has been used to demonstrate generalized laws of reflection and refraction[7–11].

Here, we show that the strong interaction between gradient metasurfaces and waveguide modes enables the demonstration of a number of device functionalities, including mode conversion, polarization rotation, perfect absorption and highly asymmetric optical power flow in waveguides. Such metasurface-based devices have substantially reduced footprints and broadband performance compared to conventional photonic integrated devices. In addition, devices based on all-dielectric metasurfaces introduce negligible insertion losses to photonic integrated circuits.

Using gradient metasurfaces to control guided waves

A gradient metasurface structure patterned on the top surface of an optical waveguide (Fig. 1) enables asymmetric coupling of waveguide modes: when an incident waveguide mode propagates against $\mathbf{k}_{\mathrm{eff}}$, the bending angle of its wavevector increases, which corresponds to coupling from lower-order into higher-order waveguide modes (Fig. 1a); conversely, when an incident waveguide mode propagates along $\mathbf{k}_{\mathrm{eff}}$, a higher-order waveguide mode is converted to a lower-order mode. If the metasurface is made of plasmonic materials, the optical power will eventually be coupled into a surface wave (Fig. 1b). The wavevector of the surface wave increases continuously, which results in enhanced confinement of the surface wave to the metasurface and progressively larger optical losses. Optical power will thus be dissipated via Joule heating in the plasmonic metasurface.

The gradient metasurface controls guided waves by strong, consecutive scattering events at the antenna array (Fig. 1a). As a result, the antennas have a collective action on the waveguide modes. Over a propagation distance of only a few times the wavelength, an effective wavevector many times larger than the phase gradient $d\Phi/dx$ can be imparted to the incident mode, resulting in a large overall wavevector change (as a comparison, gradient metasurfaces only transfer a single effective wavevector of $d\Phi/dx$ to optical waves propagating in free space). This collective effect of the gradient metasurface on guided waves enables us to substantially reduce the footprint of photonic integrated devices and simultaneously achieve broadband device performance, because of an inverse relation between device dimension and their working bandwidth[26].

An additional advantage of using metasurfaces to control waveguide modes is that the optical near-fields of nanoantennas contain both transverse electric (TE) and transverse magnetic (TM) polarized components (that is, electric-field components that are

[1]Department of Applied Physics and Applied Mathematics, Columbia University, New York, New York 10027, USA. [2]Department of Physics, The University of Texas Rio Grande Valley, Brownsville, Texas 78520, USA. [3]John A. Paulson School of Engineering and Applied Sciences, Harvard University, Cambridge, Massachusetts 02138, USA. [4]Microphotonics Center and Department of Materials Science and Engineering, Massachusetts Institute of Technology, Cambridge, Massachusetts 02139, USA. [5]Center for Functional Nanomaterials, Brookhaven National Laboratory, Upton, New York 11973, USA. †These authors contributed equally to this work. *e-mail: ny2214@columbia.edu

© 2017 Macmillan Publishers Limited, part of Springer Nature. All rights reserved.

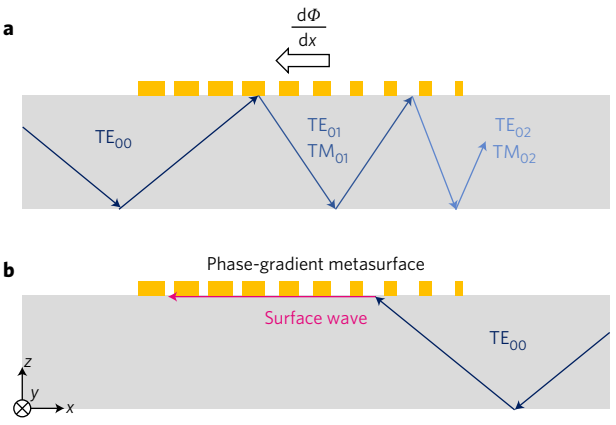

Figure 1 | Unidirectional phase gradient dΦ/dx introduced by a metasurface causes asymmetric waveguide mode coupling. a, In the forward propagation direction, an incident fundamental waveguide mode can couple into either higher-order TE or TM modes, as a result of consecutive interactions with the gradient metasurface. **b**, In the backward direction, an incident fundamental waveguide mode couples into surface waves propagating along a plasmonic gradient metasurface, and optical power is completely absorbed. TE modes are defined as waveguide modes that have their electric field component preferentially in the y direction and TM modes have their electric field component preferentially in the z direction[31,32]. The TE/TM$_{mn}$ mode has $(m+1)$ and $(n+1)$ lobes in the y and z directions, respectively.

polarized along the y and z axis, respectively, in Fig. 1). Therefore, nanoantennas are able to mediate a strong interaction between TE and TM waveguide eigenmodes, which otherwise cannot couple with each other in a bare waveguide and couple weakly in nanostructured waveguides[27–30].

Asymmetric optical power transmission in waveguides

Figure 2 shows a device that supports highly asymmetric optical power transmission around $\lambda = 2.5$ μm when the fundamental TE waveguide mode is launched along opposite propagation directions. The gradient metasurface consists of 56 gold nanorods with different lengths located on the top surface of a Si_3N_4 waveguide (Fig. 2a). Figure 2b,c shows finite-difference time-domain simulations that depict mode evolutions in two opposite propagation directions. In the forward direction, the incident TE$_{00}$ mode is converted into the TM$_{10}$ mode (Fig. 2b). In the backward direction, it couples into surface waves, and optical power is strongly absorbed (Fig. 2c), with limited reflection back into the input port or optical scattering into free space and the substrate. The lower panel of Fig. 2d shows that optical power flow bends upwards and terminates at the antenna layer on the top surface of the waveguide. The transmission of optical power in the forward and backward directions is 42.9 and 0.21%, respectively, at $\lambda = 2.50$ μm (Fig. 2e). The ratio of the transmission spectra of the two directions is maintained at a high level (>100) between $\lambda = 2.44$ μm and 2.64 μm, and reaches its peak value of ~200 at $\lambda = 2.50$ μm (Fig. 2e).

We developed a coupled-mode theory to model the highly asymmetric mode coupling in the device (Supplementary Section VIII). Figure 2f,g shows that our coupled-mode theory can accurately describe the mode evolution in both propagation directions. The most important feature of our theory that distinguishes it from conventional coupled-mode theory[31,32] is that the coefficients that govern the coupling strength between two modes are different (for example, $\kappa_{12} \neq \kappa_{21}$ for the coupling between the TE$_{00}$ and TM$_{10}$ modes and $\kappa_{13} \neq \kappa_{31}$ for the coupling between the TE$_{00}$ mode and surface waves). The physical reason for the asymmetric coupling coefficients is that the unidirectional phase gradient provided by the metasurface breaks the symmetry of optical power transfer between two modes. For example, a phase gradient dΦ/dx aligned with the light propagation direction will facilitate a higher-order waveguide mode to couple into a lower-order mode, but will inhibit the reverse process. Note that such directional waveguide mode coupling does not break time-reversal symmetry and is different from optical isolation. An optical isolator has an asymmetric scattering matrix that relates the incoming and outgoing modes at the ports connected to the device and can only be realized in systems with nonreciprocity[33], such as systems with magnetic materials[34], nonlinearity[35] or temporal refractive index modulations[36]. However, the performance of our devices is reciprocal. For example, if the TM$_{10}$ mode is launched into the right port of the device in Fig. 2a, it will be converted with high efficiency into the TE$_{00}$ mode exiting from the left port.

The devices for demonstrating asymmetric optical power flow in waveguides consist of a Y-branch waveguide and two gradient metasurface structures with opposite orientations (Fig. 3a,b). Each gradient metasurface is positioned at the centre of the top surface of one waveguide branch and consists of a phased array of gold nanorod antennas according to the design shown in Fig. 2a. In the experiment, an incident laser beam with tunable wavelengths between 2.40 and 2.50 μm and controllable polarization was coupled into the input port of the device using a single-mode mid-infrared fibre and predominantly excited the TE$_{00}$ waveguide mode. An infrared camera was used to image the output ports of the two waveguide branches and the ratio of light transmission through the two ports were monitored as a function of wavelength. Without the gradient metasurfaces, the input light is separated equally between the two branches and the two optical spots at the output ports have the same intensity. However, in devices patterned with gradient metasurfaces, we observed a large difference in light transmission through the two ports (Fig. 3c,d and Supplementary Section III). Figure 3c shows images of the two optical spots at the output ports at different wavelengths ranging from 2.43 to 2.47 μm. In the right branch, light is efficiently converted into surface waves by the gradient metasurface and optical transmission is small. In the left branch, the incident TE$_{00}$ mode is converted to the TM$_{10}$ mode, which leads to large optical transmission. The ratio of the transmission spectra reaches its peak value of ~35 around $\lambda = 2.45$ μm (Fig. 3d).

Mode converters based on plasmonic metasurfaces

Figure 4a shows a few waveguide mode converters operating around $\lambda = 4$ μm. The gradient metasurfaces consist of phased arrays of gold nanorod antennas patterned on the top surface of silicon waveguides. The incident TE fundamental waveguide mode is converted into the TM$_{00}$, TM$_{10}$ or TE$_{10}$ mode, depending on the design parameters, which include the phase gradient dΦ/dx, array length, offset of the antenna array from the waveguide centre and antenna orientation. The third column in Fig. 4a shows finite-difference time-domain simulations of mode evolution when light propagates from the left to the right through a region of the waveguide patterned with the gradient metasurfaces.

The collective action of the antennas in a gradient metasurface can be quantified by N, the number of effective wavevectors, $\mathbf{k}_{\mathrm{eff}} = \mathrm{d}\Phi/\mathrm{d}x$, imparted to the guided wave during the mode conversion process. The total additional wavevector needed for mode conversion is the difference of the propagation constants of the input and output waveguide modes, $\Delta\beta = k_o|n_{in} - n_{out}|$, where $k_o = 2\pi/\lambda_o$ is the free-space wavevector, n_{in} is the modal index of the input waveguide mode and n_{out} is the modal index of the converted waveguide mode. N is therefore defined as $N \equiv \Delta\beta/|\mathrm{d}\Phi/\mathrm{d}x|$, and can be thought of as the number of interactions between the guided wave and the metasurface, where each interaction contributes dΦ/dx to

© 2017 Macmillan Publishers Limited, part of Springer Nature. All rights reserved.

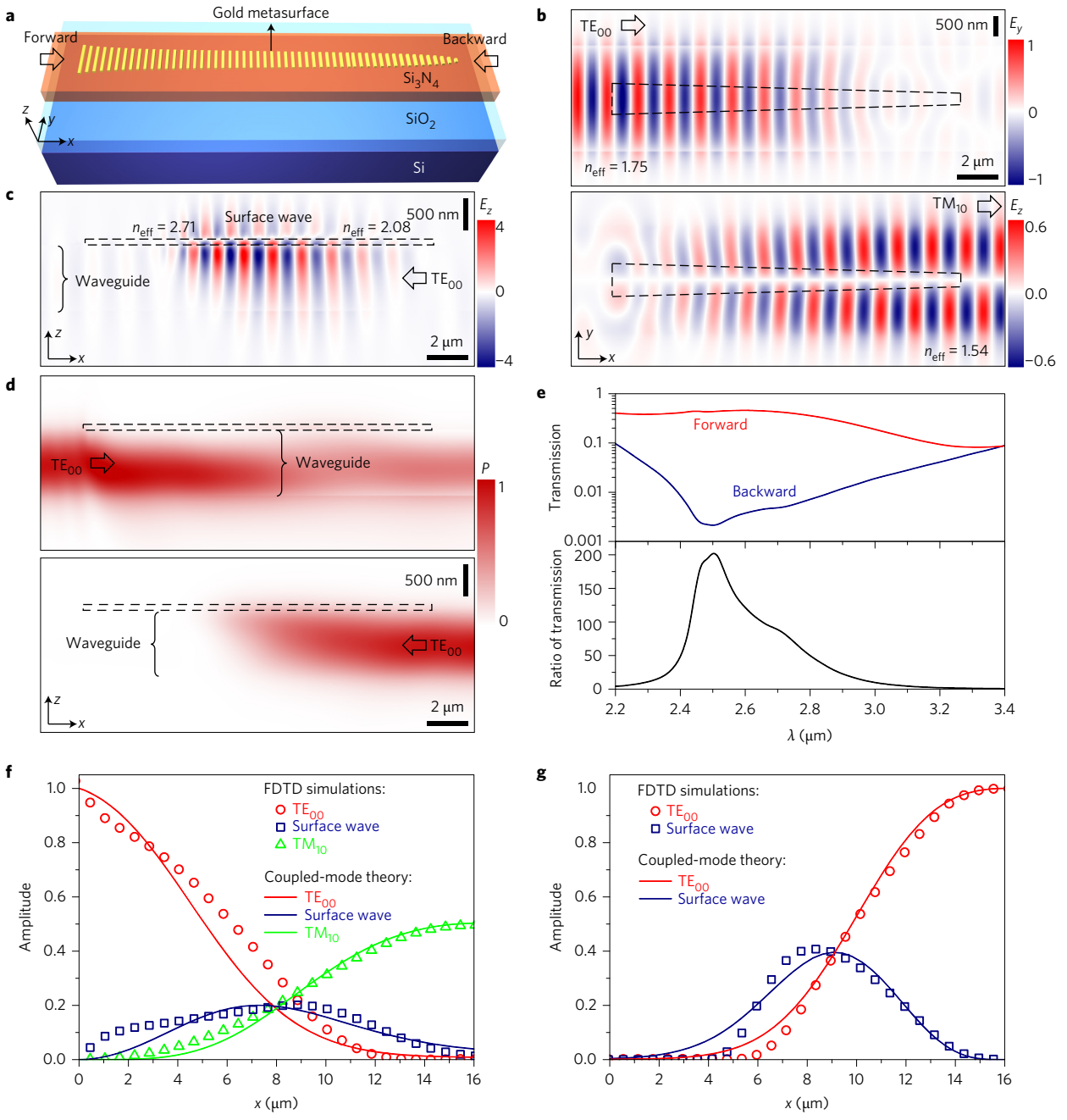

Figure 2 | Asymmetric optical power transmission in waveguides patterned with gradient metasurfaces. a, Schematic of a device working around $\lambda = 2.5$ μm. The Si_3N_4 waveguide is 2.5 μm in width and 1.0 μm in thickness. The centre-to-centre distance between adjacent antennas is 300 nm. The length of the antenna array is 16.5 μm. Detailed design parameters are provided in Supplementary Section V. **b**,**c**, Full-wave simulations showing conversion of the incident TE fundamental mode into the TM_{10} mode in the forward propagation direction and into surface waves in the backward direction. Black dashed lines indicate the location of the antenna array. Notice that the effective mode index n_{eff} evolves differently in two opposite propagation directions. **d**, Spatial distribution of the magnitude of the Poynting vector, showing highly asymmetric optical power flow as a result of the directional mode conversion. Black dashed lines indicate the location of the antenna array. **e**, Optical power transmission spectra of the device in opposite propagation directions and the ratio of the spectra, showing that highly asymmetric optical power transmission is maintained over a broad wavelength range. **f**,**g**, Mode evolution as a function of propagation distance in opposite propagation directions. The results of coupled-mode theory (curves) have good quantitative agreement with the results of full-wave simulations (symbols).

the final propagation constant. For example, the modal index decreases from 2.717 to 1.609 in the TE_{00}-to-TM_{10} mode convertor, where $d\Phi = 5.7°$ and $dx = 500$ nm, and so N is ~8.4. This large number of effective interactions between the guided wave and the metasurface occur over a propagation distance of 12 μm (the length of the antenna array), which is only ~2.9 times the free-space wavelength $\lambda_o = 4.16$ μm.

The power transmission of the mode converters is between 36 and 71%, and optical losses are mainly due to absorption in the gold nanoantennas. The purity of the converted modes can approach unity, and high-purity mode conversion can be maintained over a broad wavelength range. For example, the purity of the converted TM_{10} mode is above 90% within a wide wavelength range of $\lambda = 3.5$–5.1 μm (Fig. 4b).

© 2017 Macmillan Publishers Limited, part of Springer Nature. All rights reserved.

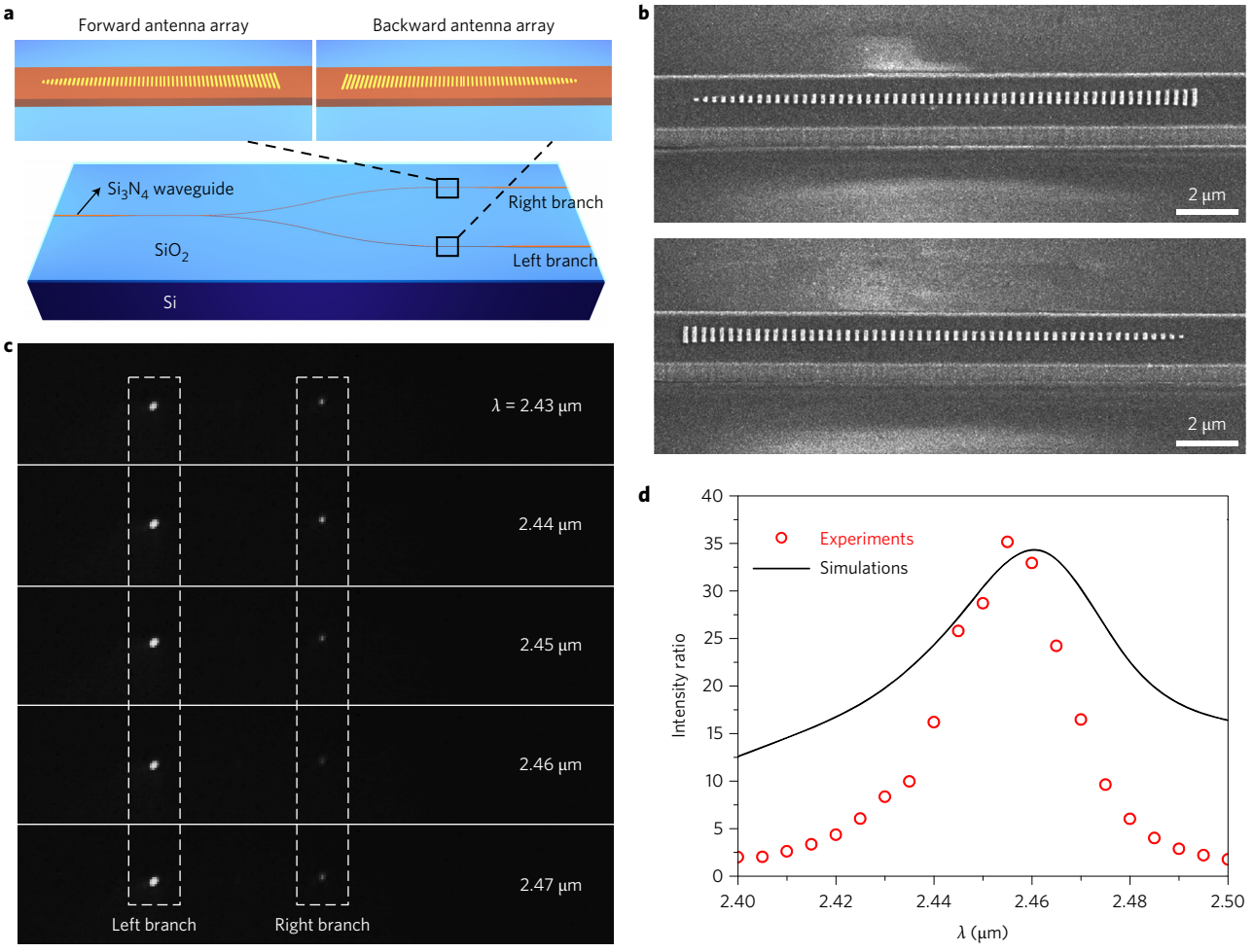

Figure 3 | Experimental demonstration of asymmetric optical power transmission in waveguides patterned with gradient metasurfaces. a, Schematic of fabricated devices consisting of a Y-branch waveguide and two gradient metasurfaces patterned on the waveguide branches. Light couples into the device from the left port as the TE_{00} mode, equally splits into the two branches, still as the TE_{00} mode, and interacts with the two gradient metasurfaces differently. Insets: zoom-in views of the device. **b**, SEM images of two gradient metasurface structures patterned on the top surfaces of the two Si_3N_4 waveguide branches of a device. The metasurface structures are arranged in two opposite orientations and each consists of 56 gold nanorod antennas with different lengths. **c**, Infrared camera images of two output ports of a device at different wavelengths ranging from 2.43 μm to 2.47 μm, showing highly asymmetric power transmission through the two waveguide branches. A polarizer was put in front of the camera to select the TM-polarized component. **d**, Measured and simulated ratios of unpolarized peak light intensity at the two output ports. The fabricated devices have slightly under-etched waveguides, which leads to a smaller wavelength range for observing asymmetric optical power flow.

Figure 5 shows the performance of a few waveguide mode converters fabricated according to the designs in Fig. 4a. We used a grating coupler to couple the output of a $\lambda = 4$ μm quantum cascade laser into the fundamental TE waveguide mode, which then interacts with gradient metasurfaces patterned on the waveguides and is converted into desired output waveguide modes. The converted modes exit from the cleaved facet at the end of the waveguides and radiate into the far-field. To characterize the converted modes, we measured their far-field profiles by raster-scanning a single-pixel indium antimonide detector in front of the waveguide output facet. Figure 5b shows that the output from the TE_{00}-to-TM_{00} mode converter (polarization rotator) has only one far-field lobe with TM polarization, and that the TE-polarized far-field is comparatively weak, indicating that the incident TE_{00} mode has been converted into the TM_{00} mode with high efficiency. The far-field profiles of the TE_{00}-to-TM_{10} and TE_{00}-to-TE_{10} mode converters have two lobes but are TM- and TE-polarized, respectively. The residual TE-polarized component in the far-field is negligible for the TE_{00}-to-TM_{10} mode converter (Fig. 5d), which indicates complete mode conversion. The far-field of the TE_{00}-to-TE_{10} mode converter (Fig. 5f) is non-ideal because of an imperfectly cleaved waveguide output facet.

Mode converters based on dielectric metasurfaces

The concept of gradient metasurfaces can be implemented in any materials systems that support optical resonances. In particular, gradient metasurfaces based on Mie resonators[37–39] allow us to substantially decrease the optical absorption associated with optical resonances and thereby reduce the insertion losses of waveguide mode converters. Figure 6a shows a few such all-dielectric mode converters operating around the telecommunications wavelength of $\lambda = 1.55$ μm. The devices consist of silicon nanorods with different lengths located on the top surface of $LiNbO_3$ waveguides. We engineered the dipolar Mie resonances supported by the silicon nanorods so that the incremental phase between adjacent elements is a constant (Supplementary Section IV).

Figure 6b–d presents scanning electron microscopy (SEM) images of a fabricated telecom TE_{00}-to-TM_{00} mode converter according to the design shown in Fig. 6a. The TE fundamental waveguide mode with tunable wavelengths between 1,480 and 1,580 nm

© 2017 Macmillan Publishers Limited, part of Springer Nature. All rights reserved.

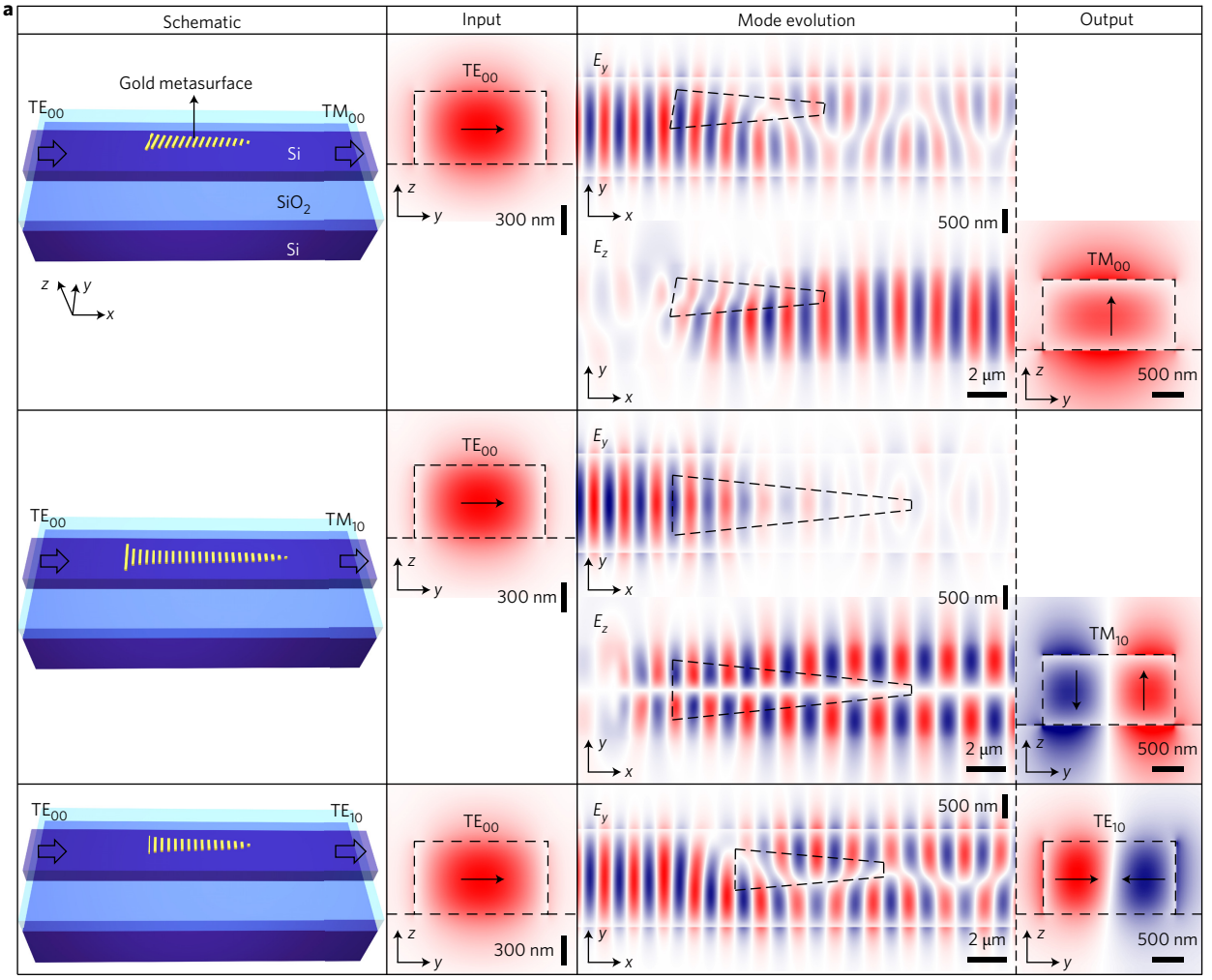

Figure 4 | Mid-infrared waveguide mode converters and polarization rotator based on plasmonic gradient metasurfaces. a, Simulated device performance. First column: device schematics. The gradient metasurfaces consist of gold phased array antennas (yellow rods) patterned on silicon waveguides and operating around $\lambda = 4$ μm. The silicon waveguides in all devices are 2.1 μm in width and 0.75 μm in thickness. The thickness of the underlying SiO_2 layer is 5 μm. The lengths of the TE_{00}-to-TM_{00}, TE_{00}-to-TM_{10} and TE_{00}-to-TE_{10} mode converters are 7.5 μm, 12 μm and 7.5 μm, respectively. Detailed design parameters of the devices are provided in Supplementary Section V. Second and fourth columns: waveguide modes at the input and output ports of the devices, respectively, with electric field components of the modes indicated by arrows. The field distributions are plotted at $\lambda = 4.50$, 4.16 and 4.10 μm, respectively, for the three devices from top to bottom in **a**. Third column: mode evolutions as light propagates from left to right. The peak transmission efficiencies of the three devices from top to bottom in **a** are, respectively, 65, 36 and 71%. The total number of effective wavevectors $\mathbf{k}_{eff} = d\Phi/dx$ imparted to the guided wave by the gradient metasurfaces during the mode conversion process is 3.5, 8.4 and 2.7, respectively, for the three devices from top to bottom in **a** (Supplementary Table 3). **b**, Purity of the converted modes as a function of wavelength, showing that the devices can operate over a broad wavelength range.

© 2017 Macmillan Publishers Limited, part of Springer Nature. All rights reserved.

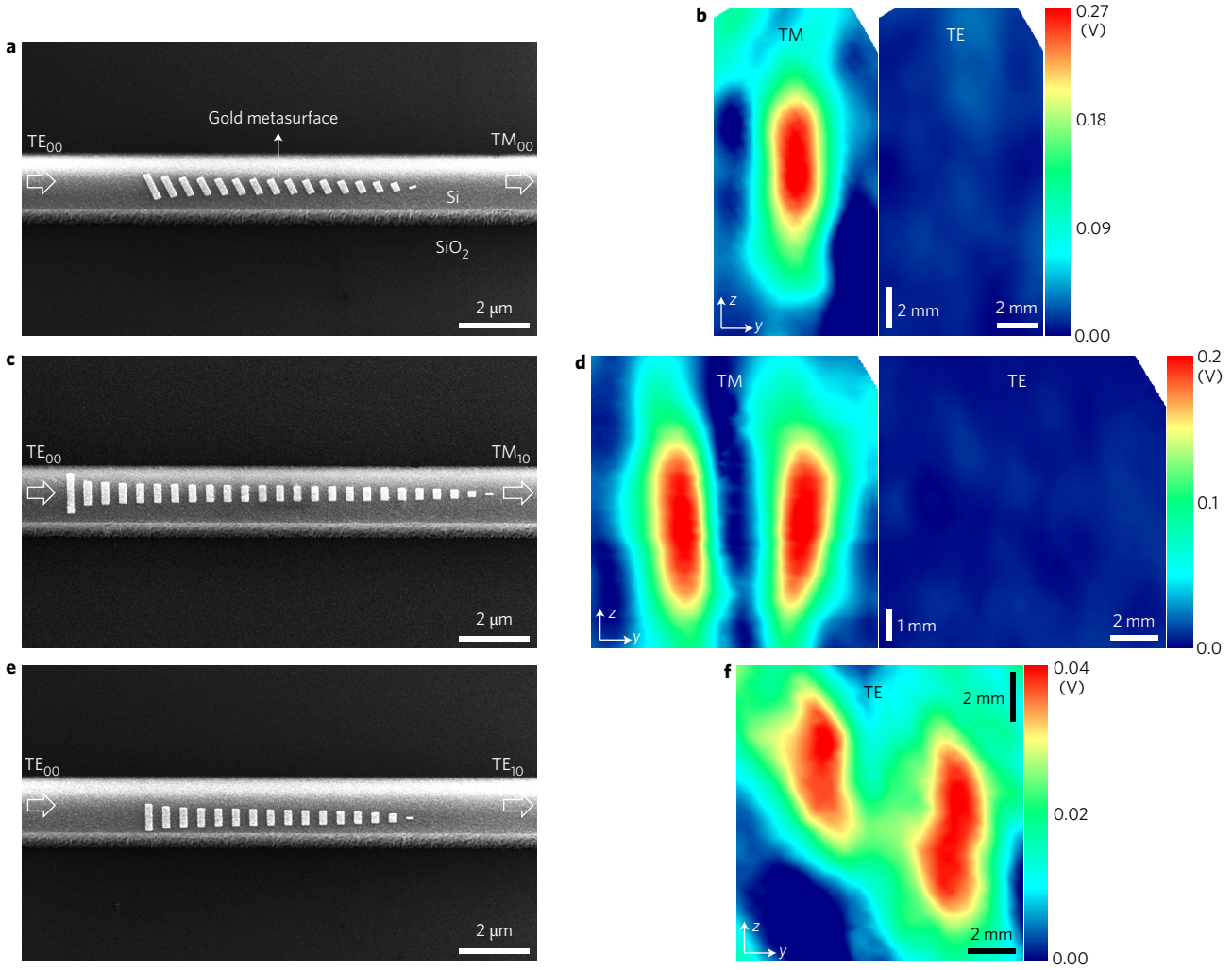

Figure 5 | Experimental demonstration of mid-infrared waveguide mode converters. a, SEM image of the TE_{00}-to-TM_{00} mode converter (perspective view, 30° from normal to the waveguide top surface). **b**, Measured far-field emission patterns of the TE_{00}-to-TM_{00} mode converter (polarization rotator), showing that the TM-polarized component has a single lobe and that the TE-polarized component is very weak. **c**, SEM image of the TE_{00}-to-TM_{10} mode converter. **d**, Measured far-field emission patterns of the TE_{00}-to-TM_{10} mode converter, showing two lobes with TM polarization and weak far-field with TE polarization. **e**, SEM image of the TE_{00}-to-TE_{10} mode converter. **f**, Measured far-field emission pattern of the TE_{00}-to-TE_{10} mode converter. The asymmetric far-field is due to defects on the cleaved waveguide output facet. The weak residual TE-polarized signal in the far-field of the TE_{00}-to-TM_{00} and TE_{00}-to-TM_{10} mode converters indicates that the conversion from the TE-polarized incident mode to the TM-polarized output modes is highly efficient. Notice that the offset of the antenna array from the waveguide central axis is chosen to be 200 nm in **a** and 400 nm in **e**, in accordance with the designs in Fig. 4a, to achieve high-purity mode conversion.

was launched into the TE_{00}-to-TM_{00} mode converters as well as into bare waveguides with the same length and cross-sectional dimensions as the mode converters. We observed no significant difference between the mode converters and the bare waveguides in their transmitted optical power, implying that the dielectric metasurfaces introduce negligible insertion losses. For example, the measured transmitted optical signal from an InGaAs photodetector for the TE_{00}-to-TM_{00} mode converters averaged over six devices is 1.09 ± 0.14 V, while the measured transmitted optical signal of 10 bare waveguides is 1.07 ± 0.19 V.

In addition, these waveguide mode converters have broadband performance. Figure 6e,f presents measured spectra of the TE- and TM-polarized components of a bare waveguide and of a TE_{00}-to-TM_{00} mode converter, respectively. The measured TE and TM components must be contributed by the TE_{00} and TM_{00} waveguide modes, respectively, because the $LiNbO_3$ waveguides are designed to only support the fundamental TE and TM modes. Thus, the spectra in Fig. 6e indicate that the TE_{00} mode is coupled into a bare waveguide and propagates along the entire length of the waveguide (2 mm), while maintaining high modal purity (>99%), and the spectra in Fig. 6f indicate that when the dielectric gradient metasurface is patterned on the waveguide, the TE_{00} mode launched into the device is converted into a high-purity TM_{00} mode (with a purity of 96% averaged over $\lambda = 1{,}480$–$1{,}580$ nm).

Conclusions

The integration of metasurface structures into photonic integrated circuits provides a highly efficient platform for the control of guided waves over broadband and with low losses. In this hybrid platform, control of waveguide modes is realized by light scattering by phased arrays of nanoantennas, where the distance between neighbouring antennas is a few times smaller than the wavelength. Optical scattering at subwavelength intervals provides the most efficient control of guided waves among all device configurations. As such, photonic integrated devices based on metasurfaces could have a footprint much smaller than conventional devices based on

© 2017 Macmillan Publishers Limited, part of Springer Nature. All rights reserved.

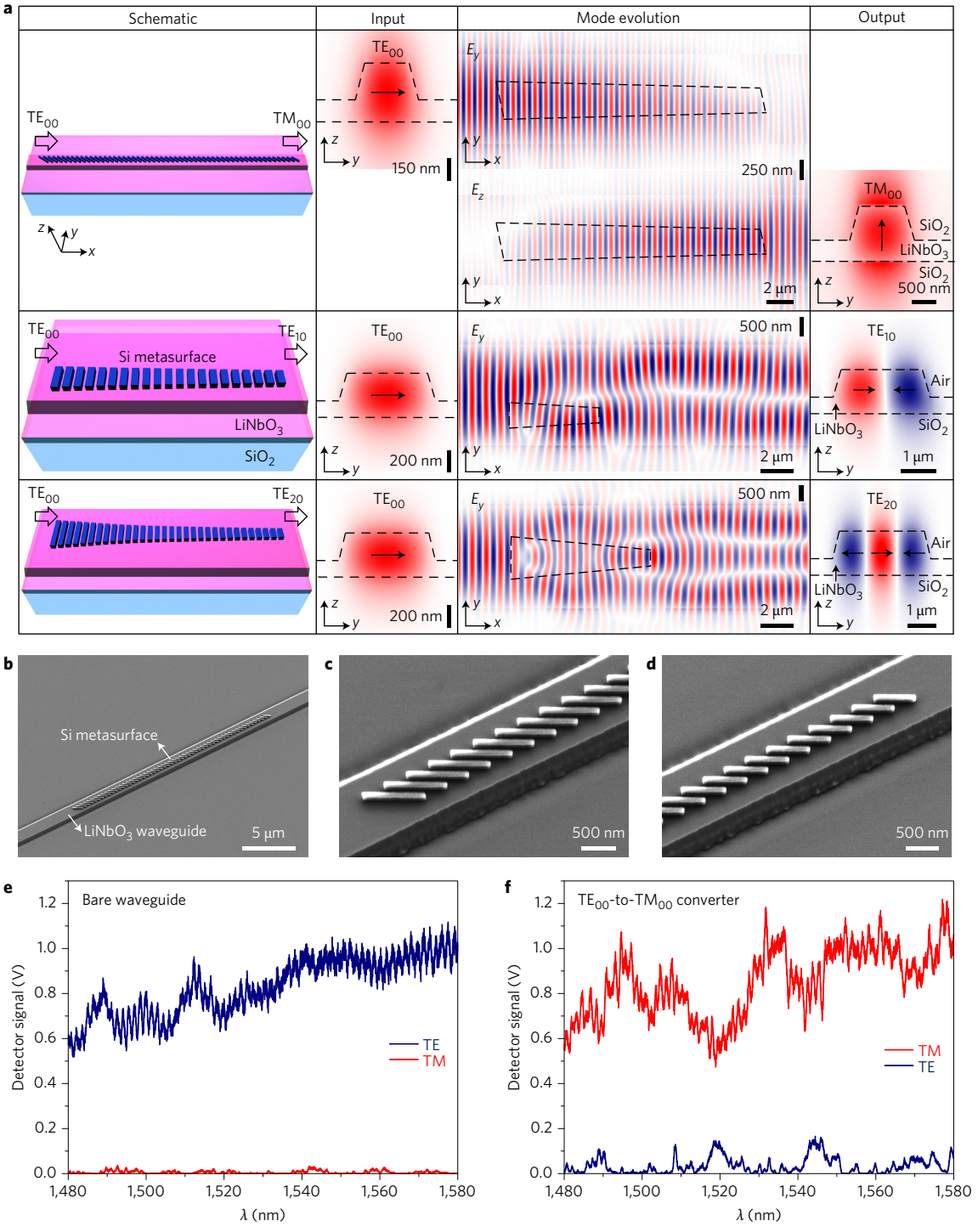

Figure 6 | Telecom waveguide mode converters based on dielectric gradient metasurfaces. a, Simulated device performance at $\lambda = 1.55$ μm. First column: schematics of three waveguide mode converters. The gradient metasurface structures consist of phased arrays of silicon antennas (dark blue rods) patterned on $LiNbO_3$ waveguides. The silicon nanorods support dipolar Mie resonances and are designed to introduce a unidirectional phase gradient along the waveguide. The lengths of the TE_{00}-to-TM_{00}, TE_{00}-to-TE_{10} and TE_{00}-to-TE_{20} mode converters are, respectively, 20.3 μm, 5.4 μm and 8.4 μm. Detailed design parameters of the devices are provided in Supplementary Section V. Second and fourth columns: waveguide modes at the input and output ports of the devices, respectively. The polarization of the electric field component of the modes is indicated by arrows and the boundaries of the $LiNbO_3$ waveguide are indicated by dashed lines. Third column: mode evolutions as light propagates from left to right. The calculated transmission efficiencies of the three devices from top to bottom averaged over $\lambda = 1{,}480$–$1{,}580$ nm are 94.4, 92.9 and 82.9%, respectively (Supplementary Section III). The total number of effective wavevectors $\mathbf{k}_{eff} = d\Phi/dx$ imparted to the guided wave by the gradient metasurfaces during the mode conversion process is 48.2, 2.6 and 4.3, respectively, for the three devices from top to bottom in **a** (Supplementary Table 4). **b**, SEM image of a fabricated TE_{00}-to-TM_{00} mode converter (before applying an overcoat of SiO_2). **c**,**d**, Zoom-in views of **b**. **e**, Measured TE- and TM-polarized components at the output port of a bare waveguide that has the same geometries (length and cross-sectional dimensions) as the TE_{00}-to-TM_{00} mode converters. **f**, Measured TE- and TM-polarized components at the output port of a TE_{00}-to-TM_{00} mode converter, showing that the device operates over a broad wavelength range and has similar power transmission to the bare waveguide.

© 2017 Macmillan Publishers Limited, part of Springer Nature. All rights reserved.

ridge waveguides (where control of light is through light propagation and coupling via weak evanescent waves) and those based on photonic crystals (where control of light is through scattering at intervals comparable to the wavelength). The compact footprint of metasurface-based photonic integrated devices could enable a higher level of device integration and a broader device operation wavelength range. In fact, the mode converters we have shown can have lengths as short as 1.7 times the free-space wavelength (for example, the mid-infrared TE_{00}-to-TE_{10} mode converter and TE_{00}-to-TM_{00} polarization rotator in Fig. 5) and can maintain high-purity mode conversion over a wavelength range as large as 35% of the central operating wavelength (Fig. 4b). Such properties are not achievable in previously demonstrated devices (for example, those based on photonic crystals[40], directional couplers[41–44], microring resonators[45], multichannel branching waveguides[46], Mach–Zehnder interferometers[47,48] and structured waveguides[27–30]), which typically have dimensions ranging from a few times to a few hundred times the free-space wavelength and work over a wavelength range less than a few percent of the central operating wavelength (Supplementary Section IX).

We envision that the functionalities demonstrated in this Article will be useful for a number of device and system applications. For example, waveguide mode conversion can be used in mode-division and polarization-division multiplexing[41,42,45,49], which can increase the capacity of optical communication channels. The conversion from waveguide modes to surface waves can be used to create broadband integrated perfect absorbers, on-chip biochemical sensors and small-footprint integrated photodetectors based on internal photoemission of hot electrons[50]. Furthermore, the unidirectional wavevector introduced by the gradient metasurfaces could be used to break the symmetry of coupling between optical pumps and generated nonlinear optical signals and thus help relax the phase-matching requirement in on-chip nonlinear wavelength conversion.

Methods

Methods and any associated references are available in the online version of the paper.

Received 1 June 2016; accepted 2 March 2017;
published online 17 April 2017

References

1. Soref, R. The past, present, and future of silicon photonics. *IEEE J. Sel. Top. Quantum Electron.* **12,** 1678–1687 (2006).
2. Soref, R. Mid-infrared photonics in silicon and germanium. *Nat. Photon.* **4,** 495–497 (2010).
3. Wada, K., Luan, H.-C., Lim, D. R. & Kimerling, L. C. On-chip interconnection beyond semiconductor roadmap: silicon microphotonics. *Proc. SPIE* **4870,** 437–443 (2002).
4. Jalali, B. & Fathpour, S. Silicon photonics. *IEEE J. Lightw. Technol.* **24,** 4600–4615 (2006).
5. Soref, R. A., Emelett, S. J. & Buchwald, W. R. Silicon waveguided components for the long-wave infrared region. *J. Opt. A* **8,** 840–848 (2006).
6. Lin, P. T. *et al.* Low-stress silicon nitride platform for mid-infrared broadband and monolithically integrated microphotonics. *Adv. Opt. Mater.* **1,** 732–739 (2013).
7. Yu, N. & Capasso, F. Flat optics with designer metasurfaces. *Nat. Mater.* **13,** 139–150 (2014).
8. Kildishev, A. V., Boltasseva, A. & Shalaev, V. M. Planar photonics with metasurfaces. *Science* **339,** 1232009 (2013).
9. Yu, N. *et al.* Flat optics: controlling wavefronts with optical antenna metasurfaces. *IEEE J. Sel. Top. Quantum Electron.* **19,** 4700423 (2013).
10. Chen, H.-T., Taylor, A. J. & Yu, N. A review of metasurfaces: physics and applications. *Rep. Prog. Phys.* **79,** 076401 (2016).
11. Yu, N. *et al.* Light propagation with phase discontinuities: generalized laws of reflection and refraction. *Science* **334,** 333–337 (2011).
12. Shitrit, N., Bretner, I., Gorodetski, Y., Kleiner, V. & Hasman, E. Optical spin Hall effects in plasmonic chains. *Nano Lett.* **11,** 2038–2042 (2011).
13. Yin, X., Ye, Z., Rho, J., Wang, Y. & Zhang, X. Photonic spin Hall effect at metasurfaces. *Science* **339,** 1405–1407 (2013).
14. Chen, X. *et al.* Dual-polarity plasmonic metalens for visible light. *Nat. Commun.* **3,** 1198 (2012).
15. Yang, Y. *et al.* Dielectric meta-reflectarray for broadband linear polarization conversion and optical vortex generation. *Nano Lett.* **14,** 1394–1399 (2014).
16. Zheng, G. *et al.* Metasurface holograms reaching 80% efficiency. *Nat. Nanotech.* **10,** 308–312 (2015).
17. Wang, Q. *et al.* Optically reconfigurable metasurfaces and photonic devices based on phase change materials. *Nat. Photon.* **10,** 60–65 (2016).
18. Vakil, A. & Engheta, N. Transformation optics using graphene. *Science* **332,** 1291–1294 (2011).
19. Gok, G. & Grbic, A. Tailoring the phase and power flow of electromagnetic fields. *Phys. Rev. Lett.* **111,** 233904 (2013).
20. Feng, L. *et al.* Experimental demonstration of a unidirectional reflectionless parity-time metamaterial at optical frequencies. *Nat. Mater.* **12,** 108–113 (2013).
21. Piggott, A. Y. *et al.* Inverse design and demonstration of a compact and broadband on-chip wavelength demultiplexer. *Nat. Photon.* **9,** 374–377 (2015).
22. Shen, B., Wang, P., Polson, R. & Menon, R. An integrated-nanophotonics polarization beamsplitter with $2.4 \times 2.4\ \mu m^2$ footprint. *Nat. Photon.* **9,** 378–382 (2015).
23. Sun, S. *et al.* Gradient-index meta-surfaces as a bridge linking propagating waves and surface waves. *Nat. Mater.* **11,** 426–431 (2012).
24. Sun, W., He, Q., Sun, S. & Zhou, L. High-efficiency surface plasmon meta-couplers: concept and microwave-regime realizations. *Light: Sci. Appl.* **5,** e16003 (2016).
25. Lin, J. *et al.* Polarization-controlled tunable directional coupling of surface plasmon polaritons. *Science* **340,** 331–334 (2013).
26. Mansuripur, M. The uncertainty principle in classical optics. *Opt. Photon. News* **13,** 44–48 (2002).
27. Holmes, B. M. & Hutchings, D. C. Realization of novel low-loss monolithically integrated passive waveguide mode converters. *IEEE Photon. Technol. Lett.* **18,** 43–45 (2006).
28. Velasco, A. V. *et al.* Ultracompact polarization converter with a dual subwavelength trench built in a silicon-on-insulator waveguide. *Opt. Lett.* **37,** 365–367 (2012).
29. Ohana, D., Desiatov, B., Mazurski, N. & Levy, U. Dielectric metasurface as a platform for spatial mode conversion in nanoscale waveguides. *Nano Lett.* **16,** 7956–7961 (2016).
30. Chen, D. *et al.* Highly efficient silicon optical polarization rotators based on mode order conversions. *Opt. Lett.* **41,** 1070–1073 (2016).
31. Yariv, A. *Optical Electronics in Modern Communications* 5th edn (Oxford Univ. Press, 1997).
32. Marcuse, D. *Theory of Dielectric Optical Waveguides* 2nd edn (Academic, 1991).
33. Jalas, D. *et al.* What is—and what is not—an optical isolator. *Nat. Photon.* **7,** 579–582 (2013).
34. Bi, L. *et al.* On-chip optical isolation in monolithically integrated non-reciprocal optical resonators. *Nat. Photon.* **5,** 758–762 (2011).
35. Fan, L. An all-silicon passive optical diode. *Science* **335,** 447–450 (2012).
36. Lira, H., Yu, Z., Fan, S. & Lipson, M. Electrically driven nonreciprocity induced by interband photonic transition on a silicon chip. *Phys. Rev. Lett.* **109,** 033901 (2012).
37. Aieta, F., Kats, M. A., Genevet, P. & Capasso, F. Multiwavelength achromatic metasurfaces by dispersive phase compensation. *Science* **347,** 1342–1345 (2015).
38. Lin, D. M., Fan, P. Y., Hasman, E. & Brongersma, M. L. Dielectric gradient metasurface optical elements. *Science* **345,** 298–302 (2014).
39. Arbabi, A., Horie, Y., Bagheri, M. & Faraon, A. Dielectric metasurfaces for complete control of phase and polarization with subwavelength spatial resolution and high transmission. *Nat. Nanotech.* **10,** 937–943 (2015).
40. Liu, V., Miller, D. A. B. & Fan, S. Ultra-compact photonic crystal waveguide spatial mode converter and its connection to the optical diode effect. *Opt. Express* **20,** 28388–28397 (2012).
41. Ding, Y. *et al.* On-chip two-mode division multiplexing using tapered directional coupler-based mode multiplexer and demultiplexer. *Opt. Express* **21,** 10376–10382 (2013).
42. Dai, D., Wang, J. & Shi, Y. Silicon mode (de)multiplexer enabling high capacity photonic networks-on-chip with a single-wavelength-carrier light. *Opt. Lett.* **38,** 1422–1424 (2013).
43. Zhang, Y. *et al.* Ultra-compact and highly efficient silicon polarization splitter and rotator. *APL Photon.* **1,** 091304 (2016).
44. Sacher, W. D., Barwicz, T., Taylor, B. J. F. & Poon, J. K. S. Polarization rotator-splitters in standard active silicon photonics platforms. *Opt. Express* **22,** 3777–3786 (2014).
45. Luo, L.-W. *et al.* WDM-compatible mode-division multiplexing on a silicon chip. *Nat. Commun.* **5,** 3069 (2014).
46. Lee, B.-T. & Shin, S.-Y. Mode-order converter in a multimode waveguide. *Opt. Lett.* **28,** 1660–1662 (2003).
47. Huang, Y., Xu, G. & Ho, S.-T. An ultracompact optical mode order converter. *IEEE Photon. Technol. Lett.* **18,** 2281–2283 (2006).

© 2017 Macmillan Publishers Limited, part of Springer Nature. All rights reserved.

48. Guan, H. *et al.* High-efficiency low-crosstalk 1310-nm polarization splitter and rotator. *IEEE Photon. Technol. Lett.* **26,** 925–928 (2014).
49. Driscoll, J. B. *et al.* Asymmetric Y junctions in silicon waveguides for on-chip mode-division multiplexing. *Opt. Lett.* **38,** 1854–1856 (2013).
50. Knight, M. W., Sobhani, H., Nordlander, P. & Halas, N. J. Photodetection with active optical antennas. *Science* **332,** 702–704 (2011).

Acknowledgements

The work was supported by the Air Force Office of Scientific Research (grant no. FA9550-14-1-0389, through a Multidisciplinary University Research Initiative programme), a Defense Advanced Research Projects Agency Young Faculty Award (grant no. D15AP00111) and the National Science Foundation (grant no. ECCS-1307948). The authors acknowledge funding from the Ministry of Defense, Singapore, and from the Defense Threat Reduction Agency (grant no. HDTRA1-13-1-0001). A.C.O. acknowledges support from the NSF IGERT programme (grant no. DGE-1069240). Research was carried out in part at the Center for Functional Nanomaterials, Brookhaven National Laboratory, which is supported by the US Department of Energy, Office of Basic Energy Sciences (contract no. DE-SC0012704). The authors thank M. Lipson, R. Osgood Jr, P.-T. Lin and L. Zhang for discussions.

Author contributions

Z.L., M.-H.K. and N.Y. conceived and designed the experiments. Z.L., M.K. and C.W. fabricated the devices, with M.L. and A.S.'s assistance. M.K., Z.L., Z.H., C.W., S.S. and A.C.O. performed the measurements and analysed the data, with A.M.A., M.L. and N.Y.'s supervision. Z.L. and M.K. developed theoretical models and conducted numerical simulations, with N.Y.'s supervision. Z.L., M.K. and N.Y. wrote the manuscript, with input from all co-authors. All authors discussed the results and commented on the manuscript.

Additional information

Supplementary information is available in the online version of the paper. Reprints and permissions information is available online at www.nature.com/reprints. Publisher's note: Springer Nature remains neutral with regard to jurisdictional claims in published maps and institutional affiliations. Correspondence and requests for materials should be addressed to N.Y.

Competing financial interests

The authors declare no competing financial interests.

© 2017 Macmillan Publishers Limited, part of Springer Nature. All rights reserved.

Methods

Design of waveguide mode converters. We tailored the 'array factor' and 'form factor' of the gradient metasurface structure to realize efficient conversion between two waveguide modes. From the perspective of ray optics, the wavevector of each waveguide mode has a characteristic bending angle (Fig. 1). Therefore, the role of the gradient metasurface should be to bend the wavevector of the incident waveguide mode by the proper amount so that the resulting wavevector matches that of a desired output waveguide mode. The incident waveguide mode interacts with the gradient metasurface many times, and each interaction bends the wavevector in accord with the magnitude and direction of the effective wavevector $\mathbf{k}_{\mathrm{eff}} = \mathrm{d}\Phi/\mathrm{d}x$. Therefore, by controlling the 'array factor' via properly choosing $\mathrm{d}\Phi/\mathrm{d}x$ and the length of the gradient metasurface, we can make sure that optical power is preferentially coupled into the desired waveguide mode.

The broadband performance of the mode converters is a result of the small device footprint. The optical analogue of the uncertainty principle prescribes that an object's spatial dimension is inversely proportional to its momentum spread in k-space[26]. Our gradient metasurface structure has a length equivalent to only a few wavelengths, so it is able to scatter an incident waveguide mode into any direction within a finite angular range that is inversely proportional to the length of the metasurface structure. The efficiency of coupling into a certain output waveguide mode will be high as long as its wavevector is within that finite angular range, and the wavevector of any other waveguide mode is outside it.

The lengths of the metasurface structures we chose range from two to about ten times the free-space wavelength. For example, the mid-infrared TE_{00}-toTM_{00} and TE_{00}-to-TE_{10} mode converters shown in Fig. 5 both have a length of 7.5 μm, which is ~1.8 times their central operating wavelength, $\lambda = 4$ μm, while the telecom TE_{00}-to-TM_{00} mode converter shown in Fig. 6b has a length of 20.3 μm, which is ~13 times its central operating wavelength, $\lambda = 1.55$ μm. The length of the metasurface structures cannot be much shorter than one free-space wavelength because, if the metasurfaces are too short, the uncertainty of the unidirectional wavevector they provide will be too large, which will prevent the realization of pure mode conversion.

In addition to the 'array factor', the selectivity of mode conversion can be enhanced by engineering the scattering pattern of individual nanoantennas (the 'form factor'). Physically, the conversion between waveguide modes is mediated by optical scattering by the antennas. Therefore, an essential condition for efficient coupling from one mode to another is that the antenna near-fields and the waveguide modes have a large spatial overlap on the waveguide cross-section. In other words,

$$\frac{\left|\iint \mathbf{E}_{\mathrm{antenna}}(y,z)\cdot\mathbf{E}^{*}_{\mathrm{wg}}(y,z)\mathrm{d}y\mathrm{d}z\right|^{2}}{\left(\iint\left|\mathbf{E}_{\mathrm{antenna}}(y,z)\right|^{2}\mathrm{d}y\mathrm{d}z\right)\cdot\left(\iint\left|\mathbf{E}_{\mathrm{wg}}(y,z)\right|^{2}\mathrm{d}y\mathrm{d}z\right)}$$

should be large. Here $\mathbf{E}_{\mathrm{antenna}}(y, z)$ represents near-fields around a single nanoantenna, $\mathbf{E}_{\mathrm{wg}}(y, z)$ is the incident or output waveguide mode, and the integration is over the waveguide transverse cross-section (that is, the y–z plane). As the antenna near-fields contain both y- and z-polarized components, the gradient metasurfaces are able to facilitate coupling between TE- and TM-polarized waveguide modes. By properly choosing the location and orientation of nanorod antennas on the top surface of the waveguide, we are able to control the value of the above integral and thus fine-tune the coupling efficiency between two waveguide modes (Supplementary Section VII).

Device fabrication. The devices were fabricated by a combination of chemical vapour deposition, electron-beam lithography and reactive ion etching. For the devices supporting asymmetric optical power transmission (Fig. 3), the Si_3N_4 films were deposited onto SiO_2/Si wafers using low-pressure chemical vapour deposition (LPCVD). For the mid-infrared waveguide mode converters (Fig. 5), the Si films were deposited onto SiO_2/Si wafers using plasma-enhanced chemical vapour deposition (PECVD). Electron-beam lithography was used to pattern gold antenna arrays and alignment marks on the Si_3N_4 or Si films. A second electron-beam lithography step was used to create etch masks to define the waveguides. Chromium was used as the etch mask for the Si_3N_4 waveguides. Polymethyl methacrylate (PMMA) electron-beam resist was used as the etch masks for defining Si waveguides. Care was taken to ensure that the antenna arrays and the waveguide etch masks were precisely aligned. Reactive ion etching was then used to etch waveguides. The etch masks were eventually removed.

The telecom waveguide mode converters (Fig. 6) were processed from lithium niobate on insulator (LNOI) wafers, which consist of lithium niobate thin films bonded onto silica substrates. Electron-beam lithography and reactive ion etching were used to first pattern lithium niobate ridge waveguides. An amorphous silicon (a-Si) layer was then deposited over the etched surface using PECVD. A second electron-beam lithography and reactive ion etching step was used to pattern the a-Si layer on the top surface of the lithium niobate waveguides into arrays of nanoantennas. The fabricated waveguides and Si nanoantennas were clad in a silica layer using PECVD. Finally, waveguide facets were diced and polished to ensure reliable and repeatable coupling efficiencies.

Detailed fabrication processes for the three types of device shown in Figs 3, 5 and 6 are described in Supplementary Section I.

Device layout and characterization. The devices that support asymmetric optical power transmission (Fig. 3) consist of a Y-branch waveguide and two gradient metasurfaces with opposite orientations. Each waveguide branch was patterned with one gradient metasurface. Linearly polarized light from a broadly tunable mid-infrared laser was butt-coupled into the input port of the devices. The guided optical power was equally split at the Y-junction and coupled into the TE fundamental waveguide mode in each of the two branches. A mid-infrared camera was used to image the optical spots at the two output ports of each Y-device. The camera images taken with a wire-grid polarizer were processed to quantify the difference in optical power transmission through the two waveguide branches.

The mid-infrared waveguide mode converters (Fig. 5) consist of a grating coupler, a waveguide taper, a narrowed segment of waveguide, a 90° waveguide turn, a segment of waveguide patterned with a gradient metasurface structure, a second waveguide taper and a cleaved facet for light outcoupling. Emission from a quantum cascade laser was collimated and focused onto the grating coupler. The narrowed segment of waveguide was used to purify the TE fundamental waveguide mode. The 90° turn in the waveguide was used to separate the signal propagating along the waveguide from the optical background guided by the silicon substrate. The incident TE_{00} mode interacts with the gradient metasurface structure and is converted into a desired output waveguide mode, which eventually radiates into the far-field from the cleaved facet at the end of the device. The converted mode was characterized by raster-scanning the far-field using a liquid-nitrogen-cooled single-pixel indium antimonide detector. A wire-grid polarizer was placed in front of the detector to characterize the polarization of the output mode.

The telecom waveguide mode converters (Fig. 6) were characterized using a butt-coupling set-up. Telecom light with tunable wavelengths was coupled into and collected from the polished facets of the lithium niobate waveguides using tapered and lensed fibres. A three-paddle fibre polarization controller was used to ensure that TE-polarized light was launched into the waveguides. The fibre-collected output light was converted into light propagating in free space and the TE and TM output polarization components were separated and detected using an InGaAs photodetector.

Detailed information on device layout and characterization is provided in Supplementary Section II.

Data availability. All relevant data are available from the corresponding author upon reasonable request.

© 2017 Macmillan Publishers Limited, part of Springer Nature. All rights reserved.